SO2 and tephra emissions during the December 22, 2018 Anak Krakatau flank-collapse eruption

Mathieu Gouhier, Raphael Paris

RESEARCH ARTICLE VOLCANICA

SO_2 and tephra emissions during the December 22, 2018 Anak Krakatau flank-collapse eruption

Mathieu Gouhier*, Raphaël Paris

Université Clermont Auvergne, CNRS, IRD, OPGC, Laboratoire Magmas et Volcans, F-63000 Clermont-Ferrand, France.

Abstract

On December 22, 2018 the south-western flank of Anak Krakatau collapsed into the sea, removing 93.8×10^6 m^3 of subaerial lavas, and generated a tsunami. Synchronously with the collapse, a large volcanic plume of SO_2 and ash (14–15 km in height) has formed, marking the onset of a paroxysmal eruption lasting from December 22, 2018 to January 06, 2019. From remote sensing analysis, we show that the eruption can be divided into three main phases. Phase I and II show both tephra and gas emissions while phase III is mostly degassing. The total amount of SO_2 injected in the atmosphere is 173±52 kt, while the minimum bulk magma volume emplaced, estimated from a topographic reconstruction, is $\sim 45 \times 10^6$ m^3. This value compares well with a petrologic-based estimate of 56.4×10^6 m^3, making the existence of external sulphur sources and sinks quite unlikely. The ice-rich ash plume formation shows that a strong sea-water/magma interaction was responsible for the phreatomagmatic activity throughout the eruption. However, we distinguish a first Vulcanian blast-derived eruption (lasting 40 min) just after the collapse having a Mass Eruption Rate (MER) of 9×10^5 kgs^{-1}, followed by a sustained lower-intensity eruption resulting in ash emissions over hours (MER = 5×10^5 kgs^{-1}). From December 23, daytime photos show typical Surtseyan activity.

Résumé

Le 22 décembre 2018, le flanc sud-ouest de l'Anak Krakatau s'est effondré dans la mer, arrachant 93.8×10^6 m^3 de roches volcaniques à l'édifice préexistant et provoquant ainsi un tsunami. Parallèlement à l'effondrement, un important panache volcanique de SO_2 et de cendres (14 à 15 km de haut) s'est formé, marquant le début d'une éruption paroxysmale qui s'est déroulée du 22 décembre 2018 au 06 janvier 2019. À partir de l'analyse des données de télédétection spatiale, on montre que l'éruption peut être divisée en trois phases principales. Les phases I et II présentent à la fois des émissions de téphra et de gaz, tandis que la phase III est essentiellement associée à du dégazage. La quantité totale de SO_2 injectée dans l'atmosphère est de 173±52 kt, tandis que le volume minimal de magma mis en place, estimé par reconstruction topographique, est de $\sim 45 \times 10^6$ m^3. Cette valeur est comparable à l'estimation basée sur la méthode pétrologique ($56{,}4 \times 10^6$ m^3), ce qui écarte l'hypothèse de sources (ou de puits) additionnelles de soufre dans le budget global de SO_2 émis en surface. La formation d'un panache de cendres riche en glace démontre une forte interaction entre l'eau de mer et le magma. Ce mécanisme est responsable de l'activité phréatomagmatique tout au long de l'éruption. Dans le détail, nous identifions une première phase Vulcanienne initiée par une explosion latérale de courte durée (~40 min) juste après l'effondrement, avec un flux de masse éruptif (MER) de 9×10^5 kgs^{-1}. Juste après, l'éruption montre une colonne plus soutenue mais de faible intensité entraînant des émissions de cendres sur plusieurs heures (MER = 5×10^5 kgs^{-1}). À partir du 23 décembre, de nombreuses photos attestent d'une activité typiquement Surtseyenne.

Keywords: SO_2 degassing; Volcanic ash; Flank Collapse; Anak Krakatau;

1 Introduction

Anak Krakatau is a volcanic island located in the Sunda Strait (Indonesia), which emerged in 1927 on the rim of the submarine caldera that was formed during the 1883 eruption of Krakatau. On December 22, 2018 at 13:50 UTC the south-western flank of Anak Krakatau volcano (Indonesia) collapsed to the sea and generated a tsunami in the Sunda Strait [ESDM 2018]. Tsunami waves devastated the coasts of Java and Sumatra, killing 431 people and damaging thousands of houses and boats, as reported by BNPB (Badan Nasional Penanggulangan Bencana: https://bnpb.go.id). Although this scenario of collapse-generated tsunami had been predicted and simulated by Giachetti et al. [2012], the disaster could not be prevented and became one of the deadliest volcanic eruptions of the last decades. After 16 months of quiescence, Anak Krakatau's activity resumed in June 2018 in the form of both explosive and effusive eruptions. The collapse followed a period of 6 months of volcanic activity and rapid growth of the volcanic cone, as evidenced by satellite images captured in 2018 (MODIS, Sentinel constellation, PlanetScope, etc.), reports on seismic activity by PVMBG (Pusat Vulkanologi dan Mitigasi

*Corresponding author: Mathieu.Gouhier@opgc.fr

Bencana Geologi: https://magma.vsi.esdm.go.id) and photographs available on the web (e.g. http://www.oysteinlundandersen.com). Immediately after the collapse, Anak Krakatau experienced a long-lived eruption, from December 22, 2018 to January 06, 2019, of intense pheatomagmatic activity showing a series of strong volcanic explosions. The amount of SO_2 and tephra released as well as the dynamics of the eruption contrast with the moderate activity of the last 6 months.

In this study, we focus on the mass budget of material emplaced during the post-collapse eruption. In particular, we provide a time-averaged estimation of bulk magma volume emitted from topographic reconstruction techniques using remote sensing data. Then, from the processing of daily UV satellite-based data, we provide a detailed analysis of SO_2 emissions. Estimates of mass fluxes of outgassed SO_2 are particularly important as they provide information on the eruptive activity at the surface [e.g. Carn and Prata 2010], the shallow plumbing system [e.g. Gauthier et al. 2016], and the magma ascent dynamics [e.g. Allard 1997]. The combination of SO_2 released at the surface with sulphur concentration in Melt Inclusions (MI) can yield key information on possible external sulphur sources and sinks at shallow levels [e.g. Edmonds et al. 2003; Sigmarsson et al. 2013]. Finally, estimation of ash plume concentration and altitude are obtained from IR satellite-based data [Prata 1989a; Wen and Rose 1994]. These parameters are critical as they allow indirect assessment of the Mass Eruption Rates (MER) of tephra emitted at the source vent from empirical formulations [Sparks et al. 1997; Mastin et al. 2009] or statistical modelling [Gouhier et al. 2019]. Also, the evaluation of airborne ash mass fluxes (Q_a) is essential in understanding the dynamics of particle transport and dispersion, and better constraining sedimentation mechanisms [e.g. Carey and Sigurdsson 1982; Durant and Rose 2009; Carazzo and Jellinek 2013; Manzella et al. 2015].

2 Data and Methods

2.1 Pre- and post-collapse topography of the island

Pre-collapse topography of Anak Island was derived from the DEMNAS (national digital elevation model of Indonesia, spatial resolution of 0.27 arc-second using the vertical datum EGM2008, provided by the Indonesian Geospatial Agency, and available at http://tides.big.go.id/DEMNAS/index.html). This DEM was built from InSAR, TerraSAR-X and ALOS-PALSAR data collected from 2000 to 2013. The original DEMNAS raster file was converted into a shapefile (contour lines) that was modified in order to include the latest growth of the edifice, as seen on photographs taken in August and November 2018 (http://www.oysteinlundandersen.com), and satellite images (e.g. Sentinel-2 image captured on 30 September 2018, and PlanetScope image captured on 17 December 2018: see Figure A1). Pre-collapse bathymetry is from Deplus et al. [1995].

The contour of the collapse scar was inferred from a Sentinel-1A image captured ~8:30 hours after the collapse (22/12/2018 at 22:33:44 UTC) and photographs taken by Susi Air flight crew the day after (23/12/2018). There is no data available on post-collapse bathymetry and the submarine extent of the collapse scar.

Intense phreatomagmatic activity rising from the sea surface inside the scar produced a significant volume of pyroclastic deposits, thus reshaping the island in a few days. Post-collapse evolution of the island's perimeter could be traced from different satellite images captured between 22 December 2018 and 31 March 2019 (Sentinel-1-A/B, Sentinel-2, TerraSAR-X, PlanetScope). The topography of the island on January 10, 2019 was reconstructed using drone photogrammetry (drone footage by James Reynolds, Earth Uncut TV: https:/www.earthuncut.tv). Images were processed using Agisoft Photoscan Pro (https:/www.agisoft.com). Using a Structure-from-Motion workflow, the software (1) detected matching points and aligned all images, (2) constructed a dense point cloud from depth information of each aligned image, (3) calculated a triangulated mesh, (4) and built a digital elevation model after 11 ground control points (GCP) were implemented (from a Sentinel 2 image captured on 13 January 2019). The resulting DEM has a resolution of 2 m per pixel, but its completeness is unequal from one flank to another due to the spatial distribution of the drone images. In order to locally complete the model, additional points were extrapolated from different aerial and ground photographs available on the web (e.g. BNPB survey of 13 January 2019). Although the method might be further optimised in the future by better parameterising the drone survey and implementing GNSS GCPs, it provides a rough estimate of the new topography of the island less than 20 days after the collapse.

2.2 Satellite-based SO_2 retrieval

Volcanic sulphur dioxide emissions (SO_2) have long been characterized from satellite-based UV sensors [e.g. Schneider et al. 1999; Carn et al. 2003; Yang et al. 2007]. A variety of sensors (IR/UV) and platforms (GEO/LEO) now exists and allows a detailed description and quantification of SO_2 mass loading during eruptive events. Firstly, in this study we used the combination of Aura/OMI data (~90 %) and Suomi-NPP/OMPS data (~10 %) in order to capture the long-term (195 days, between 10/06/2018 and 22/12/2018) SO_2 emission pattern before the Anak flank collapse. The combination of both sensors allowed us to avoid data gaps in the time series. Data were acquired from NASA's EarthData (https://search.earthdata.nasa.gov/)

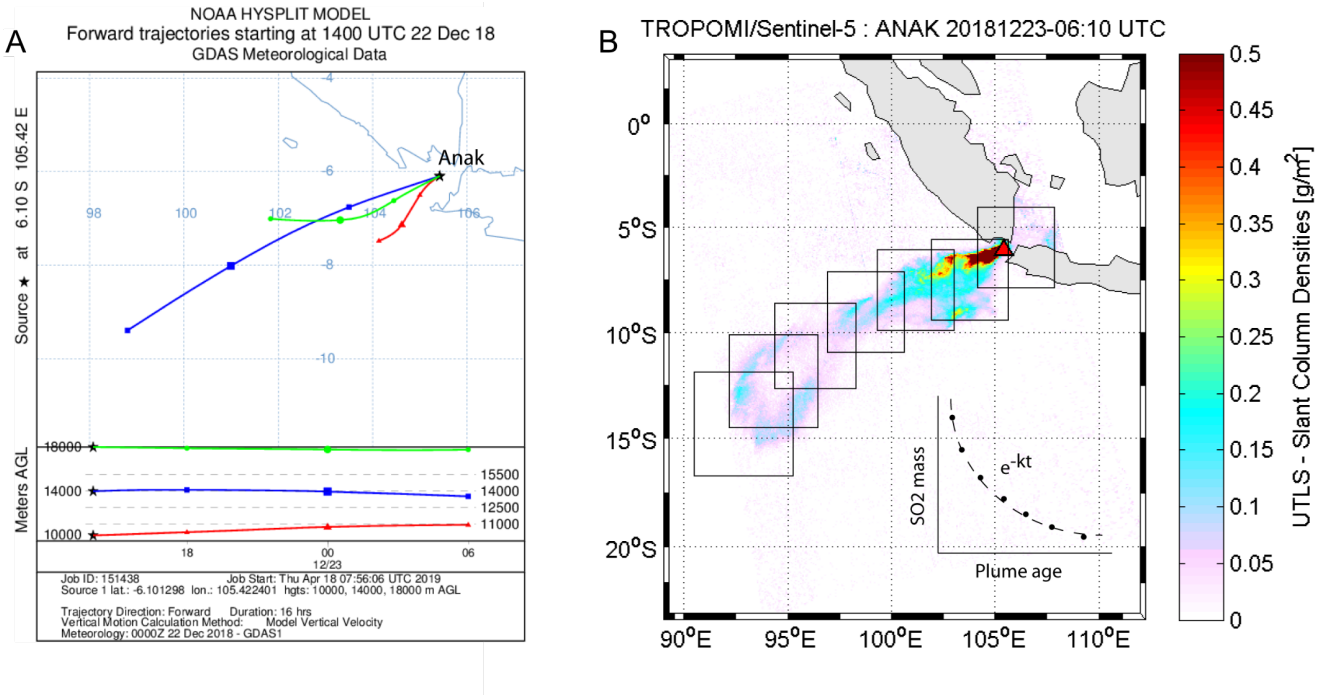

Figure 1: SO_2 mass fluxes retrieval. [A] Run example of HYSPLIT forward trajectory on 22/12/2018 at 14:00UTC showing the best trajectory (blue line) drifting in the south-westward direction at an altitude of 14 km AGL with an average velocity of 15m/s. [B] Tropomi/Sentinel-5 image on 23/12/2018 showing the SO_2 plume slant column densities (g/m^2) at UTLS level (Upper Troposphere Lower Stratosphere). Also, the boxes used for the assessment of e-folding time correction are represented.

using the "Total Column 1-orbit L2 Swath 13x24 km V003 (OMSO2)" product for OMI/Aura Sulphur Dioxide, and the "Total Column 1-Orbit L2 Swath 50x50 km" product for OMPS/NPP Sulphur Dioxide. Then, in order to better assess the eruption dynamics and provide a refined evaluation of SO_2 emissions, we processed data from the TROPOMI sensor onboard the Sentinel-5 platform. We used the Offline timeliness L2_SO2 data products from ESA-Copernicus Pre-Operation Data-Hub (https://scihub.copernicus.eu/). For estimating SO_2 emissions before the flank collapse, we used the middle troposphere elevation model (TRM, 5–10 km) as most emissions were injected to low/moderate altitudes. By contrast, for the 22/12/2018 eruption we used the 15-km elevation model (UTLS) from TROPOMI Slant Column Densities (SCD).

The calculation of the mass loadings or/and mass fluxes have already been widely described in the literature (see, e.g. Theys et al. [2013], for a review). A variety of methods associated with satellite-based data exists, such as the Traverse, Box, Delta-M or Inverse methods. They all have their specificity and domain of application. For our study we used the box method [Lopez et al. 2013] which allows mass fluxes to be determined from the estimation of SO_2 total columns divided by the duration of emission. In our case the travel time of the plume, which is directly related to the wind velocity, has been estimated from HYSPLIT trajectory model (Figure 1A). However, for large plumes extending over several hundreds of kilometres the SO_2 loss term, mainly due to the plume dilution and SO_2 oxidation into sulphuric acid, is not negligible. In the case of a significant interaction between the eruption column and the sea water, as it is most likely here, it is possible that a significant amount of SO_2 is rapidly lost to scrubbing. Finally, note that the cloud cover may have sometimes obscured and prevented SO_2 detection and quantification. This is true in particular during the pre-collapse, as weak emissions are typically of low altitude. We thus provide here a minimum estimate during this period. During the post-collapse paroxysm, a plume column altitude of ~14 km makes the SO_2 estimation much more reliable, as few or no water cloud obscuration should occur. Overall, the budget of SO_2 from a satellite image is thus a balance between SO_2 emissions and losses. This problem can be modelled from the solution of the mass conservation law:

$$\frac{\partial c}{\partial t} = -kc \tag{1}$$

where the loss term is simply assessed by the application of an age dependent correction $e^{t/\tau}$, where τ (i.e. $1/k$) is known as the SO_2 e-folding time. This parameter is difficult to assess and can be highly variable from one eruption to another [Rodríguez et al. 2008; Krotkov et al. 2010; McCormick et al. 2014; Beirle et al. 2014]. Indeed it actually depends on weather and atmospheric

conditions into which the eruption injects the gas. It will also greatly depend on plume altitude as higher atmospheric layers are much more dryer than lower ones, hence having longer lifetimes. Thus, we have calculated the SO_2 e-folding time for this eruption (Figure 1B) using a sequence of small boxes of variable sizes but enclosing the full width of the plume (i.e. crosswind). Under the simplifying, but mandatory, assumption that the flux is constant within the current plume formation, we calculate an e-folding time of τ ~30.4 hours.

2.3 Airborne ash retrieval from TIR

Satellite-based Thermal infrared (TIR) sensors are very useful for characterizing volcanic ash. In the TIR region (i.e. 7–14 µm), we can distinguish silicate particles (e.g. volcanic ash) from other aerosols (e.g. ice crystals or H_2SO_4) using a two-channel difference model based upon the absorption feature between the 11- and 12 µm) wavelengths [Prata 1989b; Wen and Rose 1994; Watson et al. 2004]. It was shown that the differences between the at-sensor "Planck" brightness temperature (referred to as BTD) observed in these two channels are negative ($-\Delta T$) for ash and positive ($+\Delta T$) for ice (Figure 2A). Building on earlier work [Prata 1989b], Wen and Rose [1994] developed a forward retrieval model that quantifies the effective radius (r_e) and optical depth (τ_c) from the extinction efficiency factor (Q_{ext}) calculated using Mie theory. This allows theoretical look-up-tables (LUT) to be generated for sets of variations of both r_e and τ_c as a function of the brightness temperature. Thus, from inverse procedures, one can retrieve a value of r_e and τ_c for any given brightness temperature pair (see Prata and Grant [2001] and Watson et al. [2004] for details), hence leading to the estimation of the vertically-integrated ash concentration ($g\,m^{-2}$) of a volcanic cloud. However, satellite retrievals are affected by several factors such as the surface characteristics (i.e. temperature and emissivity), plume geometry (i.e. altitude and thickness), ash optical properties and water vapour. These factors produce an uncertainty of ~40 % and ~30 % respectively associated with the total mass retrieval and the effective radius [Corradini et al. 2008]. Another source of uncertainty is related to the presence of large particles (typically for $r_{eff} > 6$ µm), possibly existing in fine ash clouds, which cannot be retrieved using the Mie theory because Q_{ext} does not vary strongly for $r_{eff} > \lambda/2$[Guéhenneux et al. 2015; Stevenson et al. 2015]. Overall, effects related to both misdetection issues (i.e. BTD) and the presence of coarse ash particles in the cloud may lead to a mass underestimation of about 50 % [Stevenson et al. 2015]. Also, we can provide the ash cloud top altitude (Figure 2B) using a combination of the cloud surface brightness temperature at 11.2 µm (H8 TIR waveband #02) and temperature profiles from atmospheric soundings. This technique refers to the Cloud Top Temperature (CTT) method and is only possible in the troposphere, where the temperature profile is monotonic [e.g. Prata and Grant 2001]. Here we used TIR data from Himawari-8 (H8) geostationary satellite operated by the Japan Meteorological Agency (JMA) which provides images every 10 minutes at a spatial resolution of ~ 2 × 2 km at nadir. Data were collected through the Centre for Environmental Remote Sensing (CEReS) using gridded data products from full-disc observation mode (http://www.cr.chiba-u.jp/english/database.html). The very high time resolution of TIR images used allows us to catch the dynamics of the ash plume at the initial stage, during and after the collapse (i.e. on 22/12/2018 at 13:50 UTC). In Figure 2B, we show as an example one image of the plume brightness temperature at 11.2 µm (H8 TIR waveband #02) that allows us to determine the plume top altitude between 14 and 15 km (a.s.l.) by comparing with local and synchronous atmospheric temperature profiles. For this study, temperature profiles were obtained using atmospheric sounding data of the station 96789 WIII-Jakarta (accessible from the Department of Atmospheric Science of the University of Wyoming: http://weather.uwyo.edu/upperair/sounding.html).

3 Results

3.1 Volume of post-collapse pyroclastic deposits

The flank collapse removed 93.8 × 10^6 m^3 (Figure 3) of subaerial lavas from the western flank of the volcano. This volume corresponds to a minimum value, as the submarine extent of the collapse remains unknown. However, the collapse scar was rapidly filled by post-collapse pyroclastic deposits (Figures 3 and A1). On early January imagery, the collapse headwalls are already buried by new pyroclastic deposits, and details of the pre-collapse topography such as 10 m-high coastal cliffs are no longer visible (e.g. south-eastern coast of the island). Vegetation on Panjang Island, located 2.5 km east of Anak Island, was severely damaged by ash fallout and surges, as evidenced by drone footage and Sentinel-2 images captured on January 8 and March 31, 2019 (Figure A2).

Reconstruction of post-collapse topography at two different time steps (22/12/2018: just after the collapse; and 10/01/2019: 19 days after the collapse) confirms that an important volume of juvenile tephra was deposited by ash fallouts and pyroclastic density currents after the collapse (Figure 3). On Anak Island, post-collapse pyroclastic deposits represent a volume of 29.4 × 10^6 m^3. There is no information available on the volume of submarine pyroclastic deposits. Analysis of shoreline evolution from 17 December 2018 to 31 March 2019 (Figure 4) shows a clear increase of the surface area of the island, with a shoreline progradation of up to 270 m on the eastern coast of the island. This progradation corresponds to a volume of 8.3 × 10^6 m^3

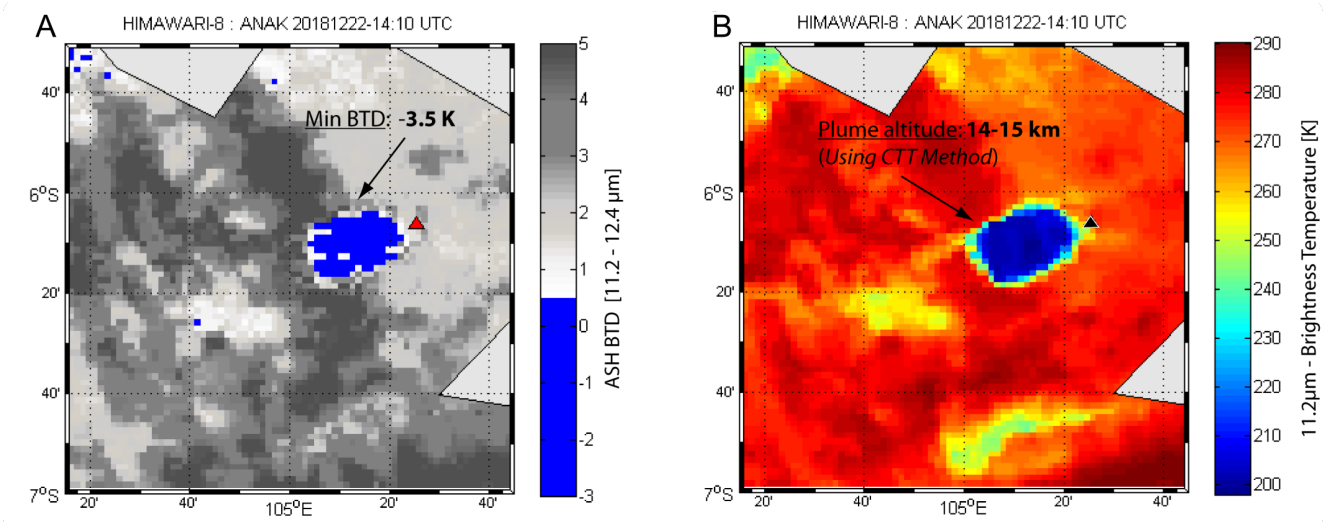

Figure 2: Ash plume characterization. [A] Brightness Temperature Difference (BTD) of band L02 (11.2 µm) and L03 (12.4 µm) from Himawari-8 satellite, showing the ash plume at 14:30 UTC on 22/12/2018. [B] Brightness Temperature (in Kelvin) at 11.2 µm used for the plume height determination (see text for details).

of submarine pyroclastic deposits, which is probably a minimum value compared to the total volume of pyroclastic deposits that were emplaced on the sea bottom. We thus estimate that the total volume of post-collapse pyroclastic deposits, both subaerial and submarine, is larger than ~45 × 10^6 m^3 (>27 × 10^6 m^3 DRE magma volume). Most of these deposits were produced in less than one week, as evidenced by satellite images captured from 23 to 29 December (Figure 4). The shoreline of the island just after the collapse (23/12/2018) is similar to the pre-collapse shoreline (17/12/2018), with the exception of the area of the collapse scar. Between 29 December 2018 and 31 March 2019, the shorelines of the island did not change significantly.

3.2 SO_2 mass loading and magma volume

In Figure 5, we processed a time series of volcanic SO_2 emitted by the Anak Krakatau in the period ranging from June 10, 2018 to January 15, 2019. These values represent the SO_2 daily mass loading (in kilotons). They have been estimated from the calculation of time-averaged mass fluxes (in kg s^{-1}, Figure 5) based on a time/distance window corresponding to the plume footprint for each image of the sequence, and referred to as the box method [Lopez et al. 2013]. It includes the e-folding time correction (τ) estimated at ~30.4 hours, and accounting for the SO_2 loss term (Figure 1). SO_2 emitted before the collapse (10/06/2018–22/12/2018) has been calculated using a combination of OMI/Aura and OMPS/Suomi satellite-based data in order to avoid data gaps. SO_2 emitted during the 22/12/2018 collapse and subsequent explosions has been calculated from TROPOMI/Sentinel-5 satellite-based data, hence allowing a refined determination of the SO_2 mass loading (see method section for details). Indeed, since early June, three main periods have been identified before the collapse. The first one spanning 30/06–04/08/2018 is associated with weak emissions of SO_2 yielding a total of 12.4 kt. A second one has been identified from 09/09 to 11/10/2018 with significantly higher SO_2 emission, and totalling 19.4 kt. Then, except a short pulse on 18–19/11/2018, no significant SO_2 emissions have been detected until the major flank collapse on 22/12/2018. The pre-collapse emissions were typically of moderate altitude (low-middle troposphere) and associated with weak to mild explosive activity (i.e. mainly Strombolian). Finally, post-collapse volcanic activity emitted 173±52 kt of SO_2 in 11 days (see inset in Figure 5). Errors on SO_2 retrieval are difficult to assess accurately, but they can be relatively large. Indeed, Lee et al. [2009] have estimated in a study dedicated to validation and error analysis that the total uncertainty in the retrieval of SO_2 columns from similar instruments is in the range of 20–40 %. The flank collapse occurred on 22/12/2018 around 13:50 UTC. This has been confirmed by thermal infrared data recorded by Himawari-8 geostationary satellite (Figure 6), allowing the full-disc image acquisition every 10 minutes. By contrast, the TROPOMI/Sentinel-5 platform provides one image/day with an acquisition time above this region lying between 06:00 and 07:00 UTC. Thus, the first peak reaching 32.3 kt of SO_2 is detected ~16 hours after the collapse (23/12/2018), hence corresponding to a time-averaged mass flux of 373.4 kg s^{-1} (Figure 5). The plume had already drifted south-westward ~1670 km away from the source vent. Processing of HYSPLIT trajectories (Figure 1) has allowed the determination of the SO_2 plume altitude at ~14 km a.s.l., which is in agreement with the ash plume altitude (14–15 km) determined from Himawari-8 TIR wavebands using the Cloud Temperature Method (CTT)

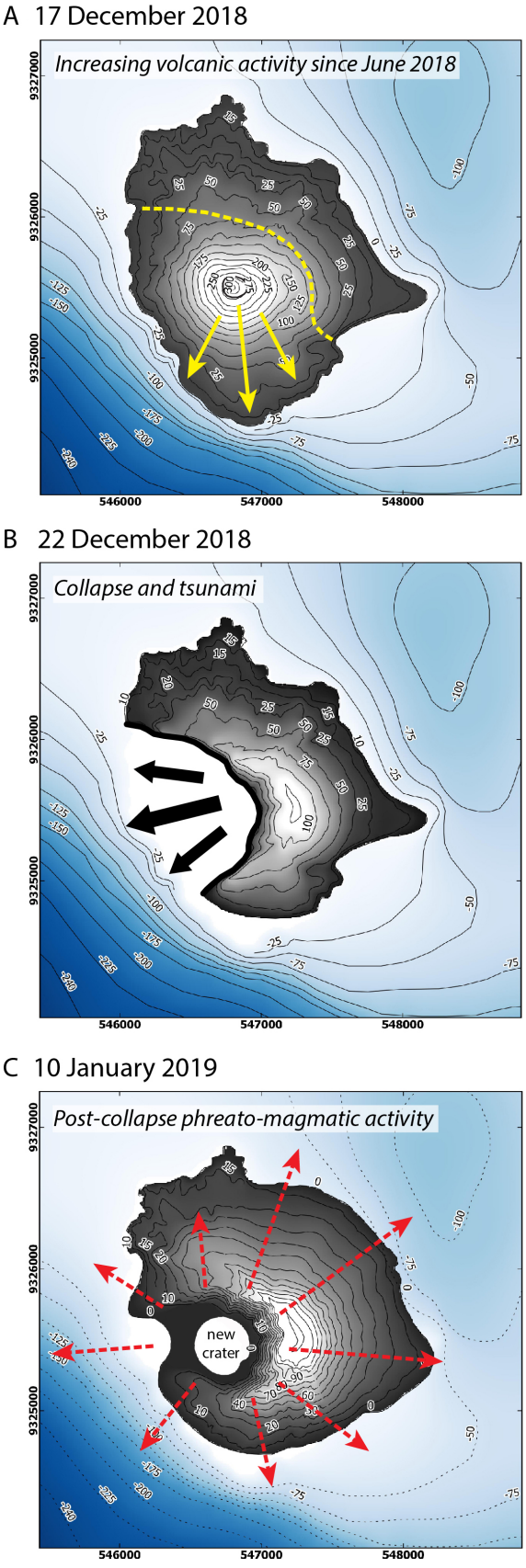

Figure 3: [Left] Evolution of the topography of Anak Krakatau volcano following the 22 December flank collapse. [A] 17 December 2018: lava flows emplaced since June 2018 (yellow arrows) are located on the south-western flank (southwest of the yellow dotted line). [B] 22 December 2018: the western flank of the active cone is truncated by a $> 93.8 \times 10^6$ m^3 collapse (black arrows). [C] 10 January 2019: rapid island growth, with $> 45 \times 10^6$m^3 of new tephra deposited on land and offshore (mostly between 22 and 29 December 2018, see Figure 5) by ash fallout and pyroclastic density currents (red arrows). UTM coordinates (zone 48S).

and atmospheric soundings (Figure 2). Such altitudes confirm a very explosive eruption, probably caused by the rapid and massive decompression of the shallow magma system due to the initial flank collapse.

From the SO_2 mass flux time series (Figure 5), we can discretize 3 different phases: the first one, including the initial flank collapse, starts on 22/12/2018 and spans 5 days of intense activity (Phase I: 22-27/12/2018), with emissions totalling 98 kt of SO_2. During the first phase, SO_2 mass fluxes gradually decrease from 373.4 to 27.5 kg s^{-1} and resumed in a strong pulse of SO_2 recorded on 28/12 with fluxes peaking at 442 kg s^{-1}. This new pulse signals the onset of the second phase, lasting only 2 days (phase II: 28-29/12/2018), and totalling 50 kt of SO_2. Finally, after 4 days of pseudo-quiescence, the third phase begins on 3 January 2019 showing lower mass fluxes (phase III: 03-06/01/2019) and with emissions totalling 25 kt of SO_2. Since then, no new emissions occured, at least within the next 2 months. Phases 2 and 3 were clearly observed on live seismograms provided

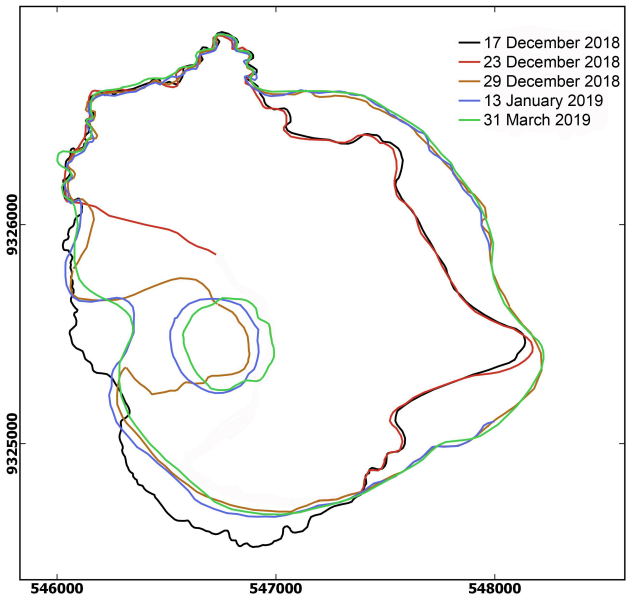

Figure 4: Shoreline evolution of Anak Island between December 2018 and March 2019 (23 December 2018 Sentinel-1A; 29 December 2018, 13 January 2019, and 31 March 2019 Sentinel-2; 17 December 2018 Planetscope data).

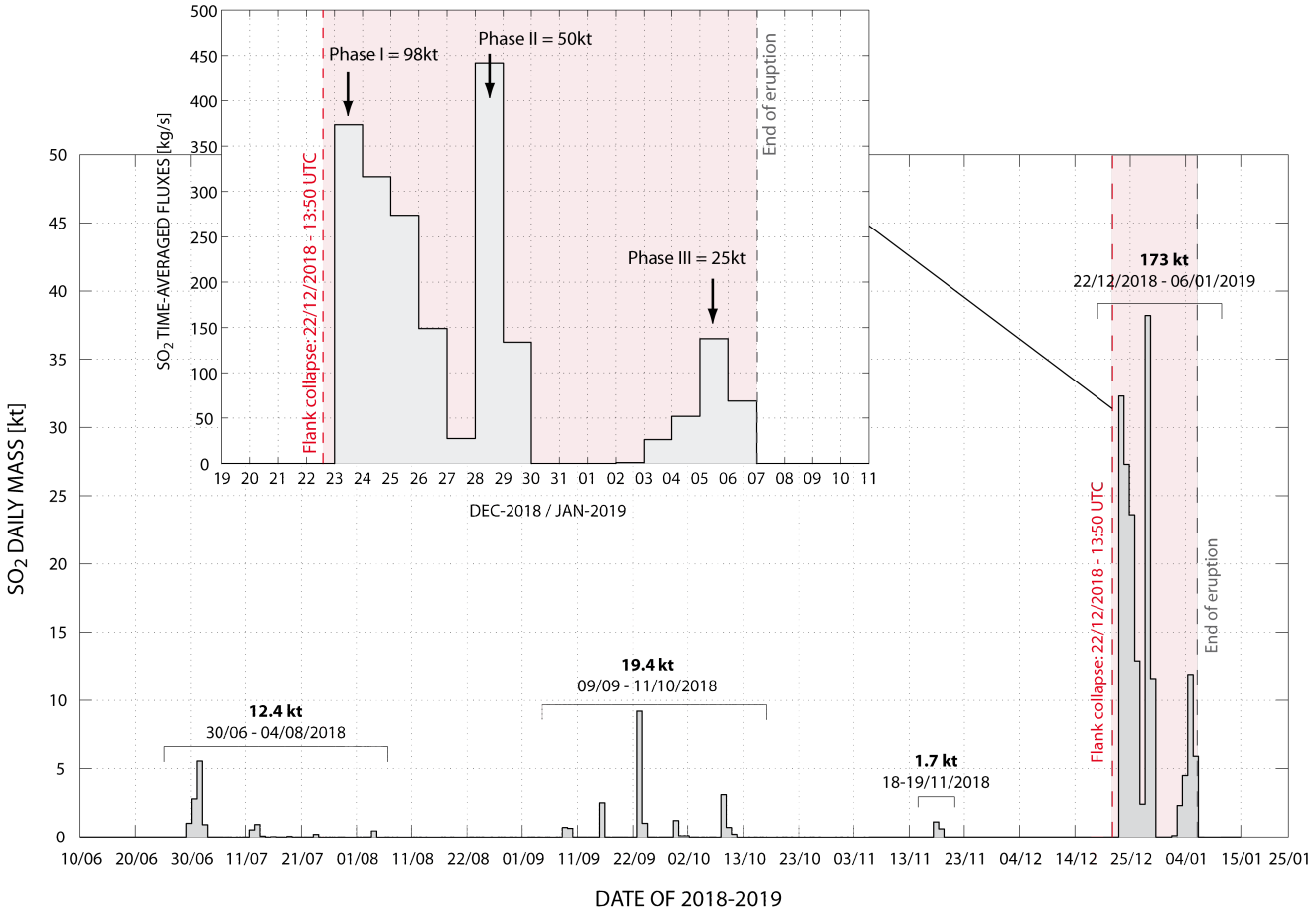

Figure 5: Daily mass of SO_2 calculated from a combination of OMI/Aura and Suomi-NPP/OMPS satellite before the collapse (10/06/2018–22/12/2018) and using Tropomi/Sentinel-5 satellite data after the collapse. Also, we provide SO_2 time-averaged mass fluxes (in $kg\,s^{-1}$) for the post-collapse eruption (top panel) clearly showing the 3 different phases of post-collapse degassing.

by PVMBG (https://magma.vsi.esdm.go.id). The three different phases following the collapse total together about 173 ±52 kt of SO_2 injected in the atmosphere.

From SO_2 degassed and measured at the surface, we can retrieve the amount of related magma involved (erupted or not) using petrologic methods [Devine et al. 1984]. For this purpose, we used the sulphur concentration of basaltic andesites reported for the 1883 Krakatau eruption [Mandeville et al. 1996; Fiege et al. 2014; Bani et al. 2015] as a reference. The average sulphur concentration in melt inclusions was found to be ~900 ppm (S_{MI}) while the average dissolved sulphur concentration in matrix glass does not exceed 10 % (S_{MG}): Calculating the concentration difference ($S_{MI} - S_{MG}$), yields an outgassed sulphur concentration of ~810 ppm. Then, from the outgassed sulphur concentration and the airborne SO_2 mass loading we can calculate the volume of parental magma, following:

$$Vol_m = \frac{M_{SO_2} \times 100}{\alpha \rho_m (S_{MI} - S_{MG})} \quad (2)$$

where M_{SO_2} is the total mass of sulphur dioxide measured by satellite (in kg), α is the molar mass ratio SO_2/S and ρ_m is the magma density taken as 2700 km^3 [Bani et al. 2015]. We have thus estimated a DRE parental magma volume of 39.5× 10^6 m^3. Using a bulk porosity of ~40 %, accounting for both erupted tephra and lava flows [Bani et al. 2015], we obtain a bulk magma volume of 65.9×10^6 m^3 (i.e. ~0.066 km^3).

By comparison, the minimum bulk volume of post-collapse pyroclastic deposits emplaced after the collapse in the proximal field (on and around Anak Island) is around ~ 45×10^6 m^3 (Figure 3). From Sentinel-2 data (Figure 4) we observe that the very large majority of this volume was already emplaced on 29 December 2018 (i.e. 7 days only after the collapse). Therefore, this bulk tephra volume can be compared with the sulphur-derived magma volume over phase I and II, solely. As a result, both volumes are quite consistent with values of 45×10^6 m^3 and 56.4×10^6 m^3 for the topographic and petrologic methods, respectively. The 20 % difference can reasonably be explained by the significant amount of tephra fallouts and PDCs lost in the sea and not visible from the topographic analysis. Also, uncertainties on input parameters used in the petrologic method combined with SO_2 retrieval er-

rors may account for this difference. The agreement between both estimations indicates that the amount of magma extruded as tephra during phase I and II is in accordance with the amount of SO_2 emitted and measured in the atmosphere. This makes the existence of external sulphur sources and sinks (e.g. sulphide globules, hydrothermal system storage) quite unlikely, at least during the first two phases (i.e. 22–29/12). Indeed, during the third phase the emission of tephra is limited, as suggested by satellite data of Anak Krakatau island contours, which do not extend after the 29/12 (Figure 4). Although some limited ash plumes remain sporadically visible, e.g. on 05/01, they cannot explain the 25 kt of SO_2 injected (i.e. equivalent to 9.5×10^6 m^3 of bulk magma for 810 ppm of outgassed sulphur) during phase III. Therefore, the SO_2 emissions during Phase III are likely mostly associated with degassing of magma in the shallow system now exposed by the flank collapse.

As most of the erupted material was in the form of tephra, it is interesting to calculate a MER averaged over the entire eruption duration. For this purpose, we take the DRE magma volume estimated from the topographic reconstruction before and after the eruption (Figure 3), which gives a minimum estimate of removed material, and the duration of phase I + II (i.e. 7 days) representing the period of active tephra emissions. This yields a MER time-averaged value of 1.2×10^5 $kg\,s^{-1}$. This is comparable to the September 26, 1997 Soufrière Hills Vulcanian eruption ($\sim 1.5 \times 10^5$ $kg\,s^{-1}$) or to the June 17, 1996 small/moderate Ruapehu eruption ($\sim 1.2 \times 10^5$ $kg\,s^{-1}$) [Gouhier et al. 2019]. Note, however, that in our case the averaged value does not account for variability of the MER possibly occurring during the 7-day averaging period.

3.3 Airborne ash mass and MER

The amount of airborne ash emitted can also be estimated from satellite-based Thermal Infra-Red (TIR) imagery provided weather conditions are favourable. For this purpose, we used data from the geostationary platform Himawari-8 providing full-disc coverage at a 10-minutes time interval (see method section for details). From the improved split window technique using the 3-bands methods [Guéhenneux et al. 2015], we first detected ash-bearing pixels. Then, from inversion of TIR data using radiative transfer modelling we give the ash cloud concentration (in $g\,m^{-2}$), as displayed in Figure 6, and the airborne ash flux Q_a (in $kg\,s^{-1}$).

From Figure 6 we observe that ash emissions can clearly be identified as early as 13:50 UTC, forming a transient high-altitude cloud of ash, coincident with the flank collapse. This first phase of effective ash emission only lasts about 40 minutes (13:50 to 14:30 UTC) and is directly related to the collapse itself. The initial plume seems to have a strong horizontal component reaching 120 km in only one hour. This has been assessed by tracking the evolution of the front edge of the plume over a sequence of Himawari-8 images. This strong horizontal component can possibly be explained by the rapid lateral decompression generated by the flank collapse oriented westward, acting as a blast-generating event. However this mechanism is not likely to be responsible for plume transport on scales of over 100 km in horizontal direction. By contrast, the front edge of the plume will likely propagate downwind at a speed higher than the wind speed as the eruption cloud expands [Sparks et al. 1986], which may also explain the high displacement velocity of the plume captured by satellite.

Note that the volcanic plume has a strong water-rich component (BTD $\gg$0), which is corroborated by daytime observations on 23/12 from detailed optical images (e.g. Terra-MODIS), and possibly preventing an accurate estimate of the ash mass loading. Thus, for this collapse-related plume we estimated a minimum airborne ash flux of $Q_a \sim 1 \times 10^4$ $kg\,s^{-1}$ using the mass difference method. Surprisingly, the ash plume emission stopped between 14:40 and 15:30 UTC, and then resumed forming a sustained high-altitude, water-rich cloud of ash for at least 10 hours. After this point, the content of water/ice in the cloud is so large that ash-containing pixels cannot be detected. This effect is enhanced by the decrease of ash emissions with time. Thus, during the first 10 hours of the post-collapse plume, a much more vertically oriented eruption column developed, still drifting in southwest direction, but at a lower velocity. Indeed, it covered only 65 km in one hour. The airborne ash flux of $Q_a \sim 5 \times 10^3$ $kg\,s^{-1}$ estimated using the mass difference method is only half that obtained during the initial blast. However, airborne ash represents only a fraction of the total amount of tephra emitted at the source vent [e.g. Rose et al. 2000; Webster et al. 2012; Gouhier et al. 2019]. Thus, in order to retrieve the total MER, one can use an empirical formulation including the plume top height [e.g. Sparks et al. 1997; Mastin et al. 2009]. But another method using both the plume height and airborne ash fluxes gives much better results [Gouhier et al. 2019], following in our case:

$$\mathrm{MER} = 25.95 Q_a^{0.72} H^{1.4} \quad (3)$$

where Q_a is the airborne fine ash flux in $kg\,s^{-1}$ and H is the top plume height (a.g.l.) in km. Using this equation, we obtain a MER of 9×10^5 $kg\,s^{-1}$ and 5×10^5 $kg\,s^{-1}$ for the collapse-related plume and the post-collapse plume, respectively (Figure 7). The eruption dynamics of both phases are quite different: the first collapse-related plume resembles a Vulcanian eruption style. The reasons for that are (i) the short duration with impulsive emissions, (ii) and the high MER compared to a moderate plume altitude [Walker 1981; Clarke et al. 2002]. The second phase lasts much longer showing sustained ash emissions over hours (at least) with a strong inter-

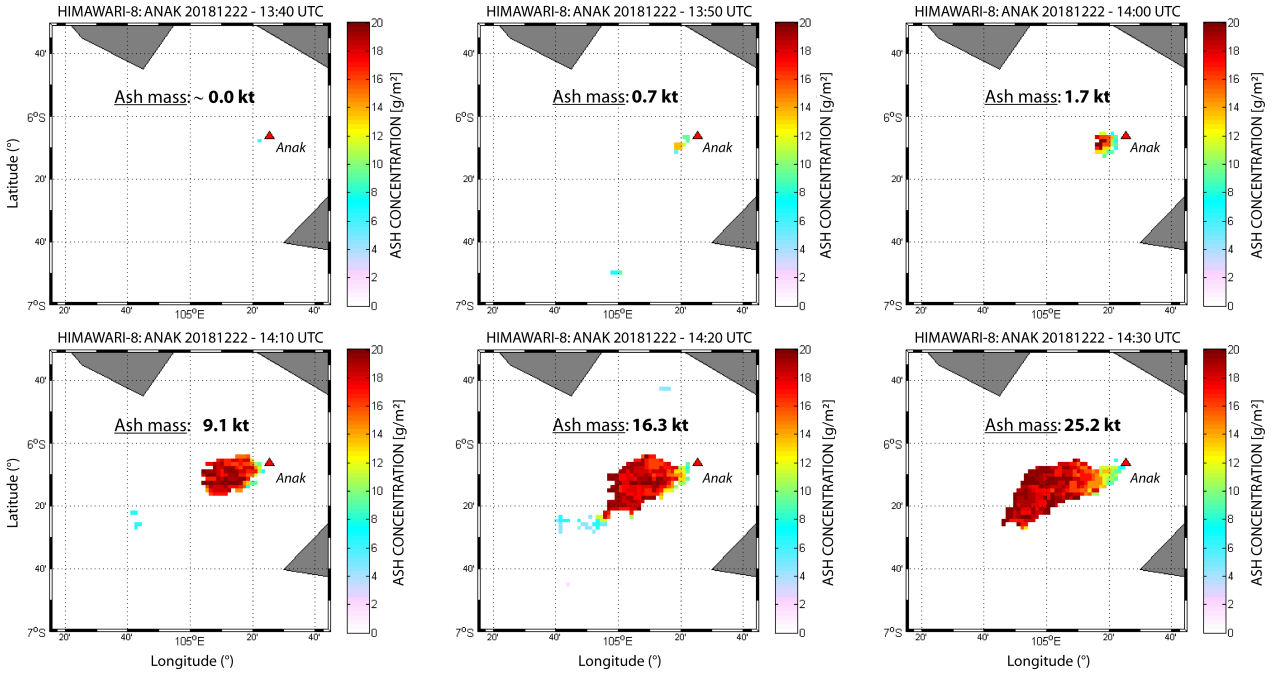

Figure 6: Airborne ash mass concentration (in $g\,m^{-2}$) retrieved from inversion of thermal infrared images using Himawari-8 data. These images show (i) the onset of the eruption at 13:50 UTC, i.e. synchronous with the collapse, (ii) the ash plume direction at a 10-minutes time resolution and (iii) the increase of the total ash mass loading.

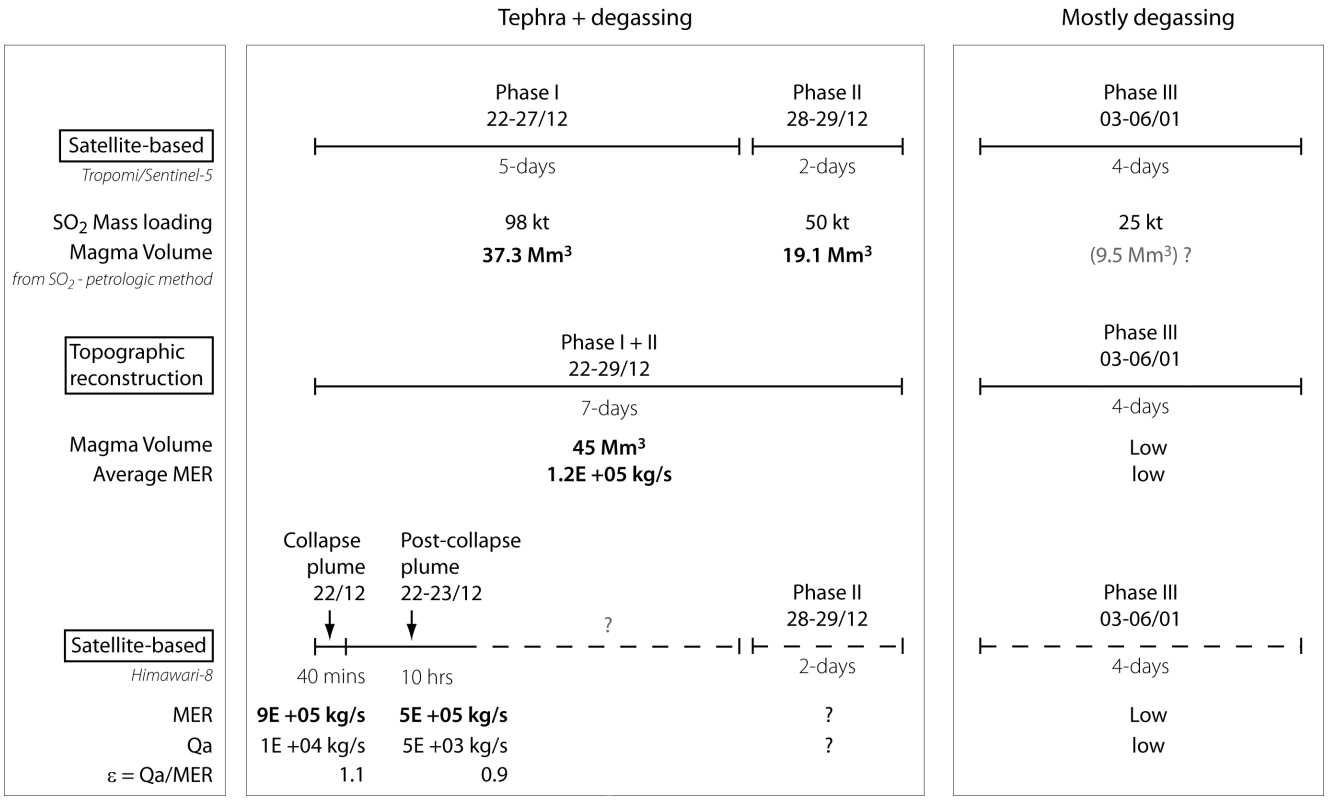

Figure 7: Main parameters for the December 2018–January 2019 eruption of Anak Krakatau summarizing the budget of material emplaced after the collapse from different techniques and spanning different time scales. "*kt*" stands for kilotons, "Mm^3" for millions of cubic meters, "MER" is Mass Eruption Rate, "Q_a" is the airborne fine ash flux, "ϵ" is the ratio between the airborne fine ash flux and the Mass Eruption Rate.

action with sea water. Daytime photos taken on 23 December, for instance, show typical Surtseyan activity (e.g. http://www.oysteinlundandersen.com). Finally, the time-averaged MER (7-days) calculated from the total volume of proximal tephra and estimated at 1.2×10^5 kg s^{-1} compares rather well with the above estimations of MER (Figure 7). Logically, the initial MER is the much higher ($\sim$ 10 times), although it is of short duration (40 min). Then the post-collapse MER, within the first 10 hours only, is still higher ($\sim$ 5 times). This leads us to believe that the MER during the last 6.5 days decreased drastically and that even periods of complete quiescence in ash emissions were perhaps possible.

4 Conclusions

The December 22, 2018 collapse-related eruption of Anak Krakatau occurred after a period of 6 months of enhanced volcanic activity and marks the climactic phase of a new eruptive cycle. Although Anak Krakatau is one of Indonesia's most active volcanoes very little information on gas emissions was available [Bani et al. 2015]. The results given in this study can be analysed in a broader perspective. Indeed, the volume of the subaerial volcanic cone of Anak Krakatau, built since 1927, has been estimated by Bani et al. [2015] during a field campaign in 2014 to be $\sim 320 \times 10^6$ m^3 (equivalent annual growth rate of 3.8×10^6 m^3 yr^{-1}). This means that the minimum estimates of the bulk volume of tephra emplaced during the 22–29/12/2018 period (45×10^6 m^3 during Phase I + II) represents the equivalent of $\sim$ 12 years of cone growth. Also, the total amount of SO_2 emitted for the whole eruption duration (173±52 kt) is significantly larger than the $\sim$70 kt yr^{-1} of SO_2 recorded at Anak Krakatau in 2014 by UV airborne spectrometer [Bani et al. 2015]. This means that the volcanic eruption produced the equivalent of 2.5 years of passive SO_2 emissions in only 11 days.

Finally, this study also shows the importance of long-term and continuous monitoring (deformation, degassing, etc.) of small volcanic islands. Collapse-related eruptions are difficult to predict, and rapid response to eruptive crises is essential for hazard mitigation. In this respect, the use of thermal infrared data onboard geostationary platforms is valuable, as it allows night and day acquisition at a time interval of 10 minutes. This is particularly important for air traffic as airborne ash may cause serious damage to aircraft potentially having dramatic consequences [Casadevall 1994].

Acknowledgements

The authors appreciated the relevant contribution of two anonymous reviewers. This is Laboratory of Excellence ClerVolc contribution no. 360. We also thank James Reynolds (Earth Uncut) for providing drone footage of Anak volcano.

Author contributions

MG processed and analyzed the Tropomi/Sentinel-5, Aura/OMI, Suomi-NPP/OMPS for SO2. MG processed HYSPLIT trajectory for the plume height and velocity determination. MG made the inversion of Infrared Himawari-8 satellite data from forward radiative transfer modelling. RP processed and analysed digital elevation models and satellite data (Sentinel-2 and PlanetScope). Both authors contributed to the preparation of the manuscript.

Data availability

Sentinel images are available on the Copernicus Open Access Hub (scihub.copernicus.eu). PlanetScope images (www.planet.com) were obtained by joining the Education and Research Program of the Planet Team (2017). Himawari-8 data, operated by the Japan Meteorological Agency (JMA), are available from the Centre for Environmental Remote Sensing (CEReS) using gridded data products.

References

Allard, P. (1997). "Endogenous magma degassing and storage at Mount Etna". *Geophysical Research Letters* 24.17, pp. 2219–2222. DOI: 10.1029/97gl02101.

Bani, P., A. Normier, C. Bacri, P. Allard, H. Gunawan, M. Hendrasto, Surono, and V. Tsanev (2015). "First measurement of the volcanic gas output from Anak Krakatau, Indonesia". *Journal of Volcanology and Geothermal Research* 302, pp. 237–241. DOI: 10.1016/j.jvolgeores.2015.07.008.

Beirle, S., C. Hörmann, M. P. de Vries, S. Dörner, C. Kern, and T. Wagner (2014). "Estimating the volcanic emission rate and atmospheric lifetime of SO&ltsub&gt2&lt/sub&gt from space: a case study for Kılauea volcano, Hawai'i". *Atmospheric Chemistry and Physics* 14.16, pp. 8309–8322. DOI: 10.5194/acp-14-8309-2014.

Carazzo, G. and A. M. Jellinek (2013). "Particle sedimentation and diffusive convection in volcanic ash-

clouds". *Journal of Geophysical Research: Solid Earth* 118.4, pp. 1420–1437. doi: 10.1002/jgrb.50155.

Carey, S. N. and H. Sigurdsson (1982). "Influence of particle aggregation on deposition of distal tephra from the May 18, 1980, eruption of Mount St. Helens volcano". *Journal of Geophysical Research: Solid Earth* 87.B8, pp. 7061–7072. doi: 10.1029/jb087ib08p07061.

Carn, S. A., A. J. Krueger, G. J. S. Bluth, S. J. Schaefer, N. A. Krotkov, I. M. Watson, and S. Datta (2003). "Volcanic eruption detection by the Total Ozone Mapping Spectrometer (TOMS) instruments: a 22-year record of sulphur dioxide and ash emissions". *Geological Society, London, Special Publications* 213.1, pp. 177–202. doi: 10.1144/gsl.sp.2003.213.01.11.

Carn, S. A. and F. J. Prata (2010). "Satellite-based constraints on explosive SO2release from Soufrière Hills Volcano, Montserrat". *Geophysical Research Letters* 37.19. doi: 10.1029/2010gl044971.

Casadevall, T. J. (1994). *Volcanic ash and aviation safety: proceedings of the First international symposium on Volcanic ash and aviation safety*. Tech. rep. doi: 10.3133/b2047.

Clarke, A. B., B. Voight, A. Neri, and G. Macedonio (2002). "Transient dynamics of vulcanian explosions and column collapse". *Nature* 415.6874, pp. 897–901. doi: 10.1038/415897a.

Corradini, S., C. Spinetti, E. Carboni, C. Tirelli, M. F. Buongiorno, S. Pugnaghi, and G. Gangale (2008). "Mt. Etna tropospheric ash retrieval and sensitivity analysis using Moderate Resolution Imaging Spectroradiometer measurements". *Journal of Applied Remote Sensing* 2.1, p. 023550. doi: 10.1117/1.3046674.

Deplus, C., S. Bonvalot, D. Dahrin, M. Diament, H. Harjono, and J. Dubois (1995). "Inner structure of the Krakatau volcanic complex (Indonesia) from gravity and bathymetry data". *Journal of Volcanology and Geothermal Research* 64.1-2, pp. 23–52. doi: 10.1016/0377-0273(94)00038-i.

Devine, J. D., H. Sigurdsson, A. N. Davis, and S. Self (1984). "Estimates of sulfur and chlorine yield to the atmosphere from volcanic eruptions and potential climatic effects". *Journal of Geophysical Research: Solid Earth* 89.B7, pp. 6309–6325. doi: 10.1029/jb089ib07p06309.

Durant, A. J. and W. I. Rose (2009). "Sedimentological constraints on hydrometeor-enhanced particle deposition: 1992 Eruptions of Crater Peak, Alaska". *Journal of Volcanology and Geothermal Research* 186.1-2, pp. 40–59. doi: 10.1016/j.jvolgeores.2009.02.004.

Edmonds, M., C. Oppenheimer, D. Pyle, R. Herd, and G. Thompson (2003). "SO2 emissions from Soufrière Hills Volcano and their relationship to conduit permeability, hydrothermal interaction and degassing regime". *Journal of Volcanology and Geothermal Research* 124.1-2, pp. 23–43. doi: 10.1016/s0377-0273(03)00041-6.

Fiege, A., F. Holtz, N. Shimizu, C. W. Mandeville, H. Behrens, and J. L. Knipping (2014). "Sulfur isotope fractionation between fluid and andesitic melt: An experimental study". *Geochimica et Cosmochimica Acta* 142, pp. 501–521. doi: 10.1016/j.gca.2014.07.015.

Gauthier, P.-J., O. Sigmarsson, M. Gouhier, B. Haddadi, and S. Moune (2016). "Elevated gas flux and trace metal degassing from the 2014-2015 fissure eruption at the Bárðarbunga volcanic system, Iceland". *Journal of Geophysical Research: Solid Earth* 121.3, pp. 1610–1630. doi: 10.1002/2015jb012111.

Giachetti, T., R. Paris, K. Kelfoun, and B. Ontowirjo (2012). "Tsunami hazard related to a flank collapse of Anak Krakatau Volcano, Sunda Strait, Indonesia". *Geological Society, London, Special Publications* 361.1, pp. 79–90. doi: 10.1144/sp361.7.

Gouhier, M., J. Eychenne, N. Azzaoui, A. Guillin, M. Deslandes, M. Poret, A. Costa, and P. Husson (2019). "Low efficiency of large volcanic eruptions in transporting very fine ash into the atmosphere". *Scientific Reports* 9.1. doi: 10.1038/s41598-019-38595-7.

Guéhenneux, Y., M. Gouhier, and P. Labazuy (2015). "Improved space borne detection of volcanic ash for real-time monitoring using 3-Band method". *Journal of Volcanology and Geothermal Research* 293, pp. 25–45. doi: 10.1016/j.jvolgeores.2015.01.005.

Kementerian Energi dan Sumber Daya Mineral [Ministry of Energy and Mineral Resources] (2018). *Surat Kaban Laporan Gunung Anak Krakatau – Report on the activity of Anak Krakatau volcano, 31 December 2018*. Tech. rep.

Krotkov, N. A., M. R. Schoeberl, G. A. Morris, S. Carn, and K. Yang (2010). "Dispersion and lifetime of the SO2cloud from the August 2008 Kasatochi eruption". *Journal of Geophysical Research* 115. doi: 10.1029/2010jd013984.

Lee, C., R. V. Martin, A. van Donkelaar, G. O'Byrne, N. Krotkov, A. Richter, L. G. Huey, and J. S. Holloway (2009). "Retrieval of vertical columns of sulfur dioxide from SCIAMACHY and OMI: Air mass factor algorithm development, validation, and error analysis". *Journal of Geophysical Research* 114.D22. doi: 10.1029/2009jd012123.

Lopez, T., S. Carn, C. Werner, D. Fee, P. Kelly, M. Doukas, M. Pfeffer, P. Webley, C. Cahill, and D. Schneider (2013). "Evaluation of Redoubt Volcano's sulfur dioxide emissions by the Ozone Monitoring Instrument". *Journal of Volcanology and Geothermal Research* 259, pp. 290–307. doi: 10.1016/j.jvolgeores.2012.03.002.

Mandeville, C. W., S. Carey, and H. Sigurdsson (1996). "Magma mixing, fractional crystallization and volatile degassing during the 1883 eruption of Krakatau volcano, Indonesia". *Journal of Volcanology and Geothermal Research* 74.3-4, pp. 243–274. doi: 10.1016/s0377-0273(96)00060-1.

Manzella, I., C. Bonadonna, J. C. Phillips, and H. Monnard (2015). "The role of gravitational instabilities in deposition of volcanic ash". *Geology* 43.3, pp. 211–214. DOI: 10.1130/g36252.1.

Mastin, L. et al. (2009). "A multidisciplinary effort to assign realistic source parameters to models of volcanic ash-cloud transport and dispersion during eruptions". *Journal of Volcanology and Geothermal Research* 186.1-2, pp. 10–21. DOI: 10.1016/j.jvolgeores.2009.01.008.

McCormick, B. T., M. Herzog, J. Yang, M. Edmonds, T. A. Mather, S. A. Carn, S. Hidalgo, and B. Langmann (2014). "A comparison of satellite- and ground-based measurements of SO2emissions from Tungurahua volcano, Ecuador". *Journal of Geophysical Research: Atmospheres* 119.7, pp. 4264–4285. DOI: 10.1002/2013jd019771.

Prata, A. J. (1989a). "Infrared radiative transfer calculations for volcanic ash clouds". *Geophysical Research Letters* 16.11, pp. 1293–1296. DOI: 10.1029/g1016i011p01293.

Prata, A. J. and I. F. Grant (2001). "Retrieval of microphysical and morphological properties of volcanic ash plumes from satellite data: Application to Mt Ruapehu, New Zealand". *Quarterly Journal of the Royal Meteorological Society* 127.576, pp. 2153–2179. DOI: 10.1002/qj.49712757615.

Prata, A. (1989b). "Observations of volcanic ash clouds in the 10-12 μm window using AVHRR/2 data". *International journal of Remote sensing* 10.4-5, pp. 751–761. DOI: 10.1080/01431168908903916.

Rodrıguez, L. A., I. M. Watson, M. Edmonds, G. Ryan, V. Hards, C. M. Oppenheimer, and G. J. Bluth (2008). "SO2 loss rates in the plume emitted by Soufrière Hills volcano, Montserrat". *Journal of Volcanology and Geothermal Research* 173.1-2, pp. 135–147. DOI: 10.1016/j.jvolgeores.2008.01.003.

Rose, W. I., G. J. S. Bluth, and G. G. J. Ernst (2000). "Integrating retrievals of volcanic cloud characteristics from satellite remote sensors: a summary". *Philosophical Transactions of the Royal Society of London. Series A: Mathematical, Physical and Engineering Sciences* 358.1770. Ed. by P. Francis, J. Neuberg, and R. S. J. Sparks, pp. 1585–1606. DOI: 10.1098/rsta.2000.0605.

Schneider, D. J., W. I. Rose, L. R. Coke, G. J. S. Bluth, I. E. Sprod, and A. J. Krueger (1999). "Early evolution of a stratospheric volcanic eruption cloud as observed with TOMS and AVHRR". *Journal of Geophysical Research: Atmospheres* 104.D4, pp. 4037–4050. DOI: 10.1029/1998jd200073.

Sigmarsson, O., B. Haddadi, S. Carn, S. Moune, J. Gudnason, K. Yang, and L. Clarisse (2013). "The sulfur budget of the 2011 Grımsvötn eruption, Iceland". *Geophysical Research Letters* 40.23, pp. 6095–6100. DOI: 10.1002/2013gl057760.

Sparks, R. J., J. G. Moore, and C. J. Rice (1986). "The initial giant umbrella cloud of the May 18th, 1980, explosive eruption of Mount St. Helens". *Journal of Volcanology and Geothermal Research* 28.3-4, pp. 257–274. DOI: 10.1016/0377-0273(86)90026-0.

Sparks, R. S. J., M. Bursik, S. Carey, J. Gilbert, L. Glaze, H. Sigurdsson, and A. Woods (1997). *Volcanic plumes*. Wiley.

Stevenson, J., S. Millington, F. Beckett, G. Swindles, and T. Thordarson (2015). "Big grains go far: understanding the discrepancy between tephrochronology and satellite infrared measurements of volcanic ash". *Atmospheric Measurement Techniques* 8.5, pp. 2069–2091. DOI: 10.5194/amt-8-2069-2015.

Theys, N. et al. (2013). "Volcanic SO2 fluxes derived from satellite data: a survey using OMI, GOME-2, IASI and MODIS". *Atmospheric Chemistry and Physics* 13.12, pp. 5945–5968. DOI: 10.5194/acp-13-5945-2013.

Walker, G. P. (1981). "Generation and dispersal of fine ash and dust by volcanic eruptions". *Journal of Volcanology and Geothermal Research* 11.1, pp. 81–92. DOI: 10.1016/0377-0273(81)90077-9.

Watson, I., V. Realmuto, W. Rose, A. Prata, G. Bluth, Y. Gu, C. Bader, and T. Yu (2004). "Thermal infrared remote sensing of volcanic emissions using the moderate resolution imaging spectroradiometer". *Journal of Volcanology and Geothermal Research* 135.1-2, pp. 75–89. DOI: 10.1016/j.jvolgeores.2003.12.017.

Webster, H. N. et al. (2012). "Operational prediction of ash concentrations in the distal volcanic cloud from the 2010 Eyjafjallajökull eruption". *Journal of Geophysical Research: Atmospheres* 117.D20. DOI: 10.1029/2011jd016790.

Wen, S. and W. I. Rose (1994). "Retrieval of sizes and total masses of particles in volcanic clouds using AVHRR bands 4 and 5". *Journal of Geophysical Research* 99.D3, p. 5421. DOI: 10.1029/93jd03340.

Yang, K., N. A. Krotkov, A. J. Krueger, S. A. Carn, P. K. Bhartia, and P. F. Levelt (2007). "Retrieval of large volcanic SO2 columns from the Aura Ozone Monitoring Instrument: Comparison and limitations". *Journal of Geophysical Research: Atmospheres* 112.D24. DOI: 10.1029/2007JD008825.

A Appendix 1

Supplementary figures (Figure A1 and Figure A2).

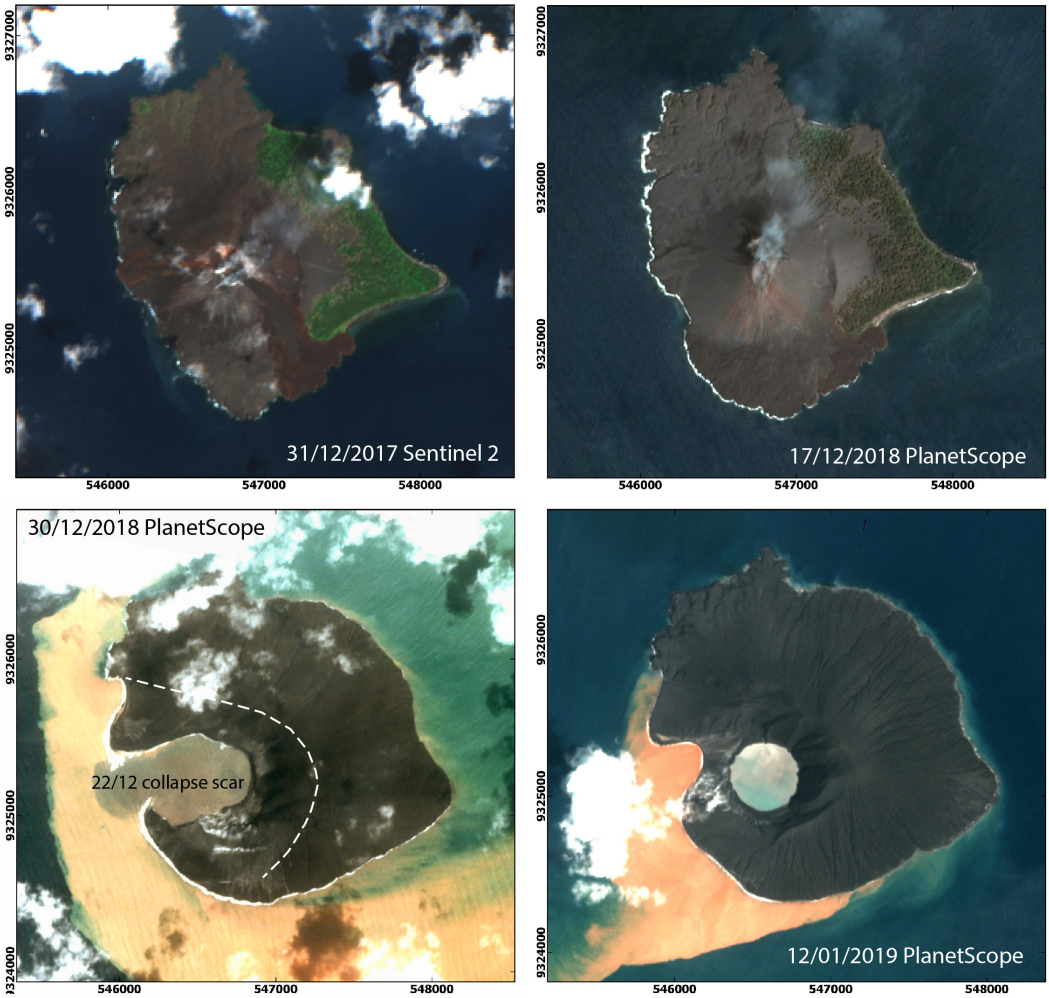

Figure A1: Evolution of the island of Anak Krakatau from December 2017 to January 2019, as seen from satellite imagery (Sentinel-2 and PlanetScope).

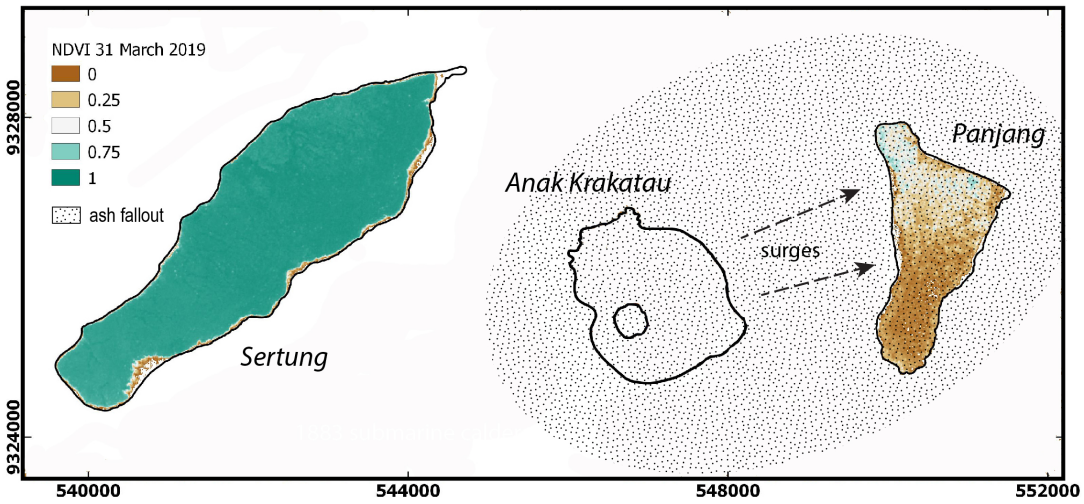

Figure A2: NDVI (Normalized Difference Vegetation Index) calculated from bands 4 (red) and 8 (NIR) of a Sentinel-2B image captured on 31 March 2019, showing loss of vitality of vegetation on Panjang Island due to successive ash plume fallouts and pyroclastic surges after the 22 December 2018 flank collapse (as shown on photographs captured on 23 December 2018).